ACS APPLIED MATERIALS & INTERFACES

Research Article

www.acsami.org

Surface-Tuned Co_3O_4 Nanoparticles Dispersed on Nitrogen-Doped Graphene as an Efficient Cathode Electrocatalyst for Mechanical Rechargeable Zinc–Air Battery Application

Santosh K. Singh,[†,‡] Vishal M. Dhavale,[†,‡] and Sreekumar Kurungot*[,†,‡]

[†]Physical and Materials Chemistry Division, CSIR-National Chemical Laboratory, Dr. Homi Bhabha Road, Pune 411008, India

[‡]Academy of Scientific and Innovative Research, Anusandhan Bhawan, 2 Rafi Marg, New Delhi 110 001, India

Supporting Information

ABSTRACT: The most vital component of the fuel cells and metal–air batteries is the electrocatalyst, which can facilitate the oxygen reduction reaction (ORR) at a significantly reduced overpotential. The present work deals with the development of surface-tuned cobalt oxide (Co_3O_4) nanoparticles dispersed on nitrogen-doped graphene as a potential ORR electrocatalyst possessing some unique advantages. The thermally reduced nitrogen-doped graphene (NGr) was decorated with three different morphologies of Co_3O_4 nanoparticles, viz., cubic, blunt edged cubic, and spherical, by using a simple hydrothermal method. We found that the spherical Co_3O_4 nanoparticle supported NGr catalyst (Co_3O_4–SP/NGr-24h) has acquired a significant activity makeover to display the ORR activity closely matching with the state-of-the-art Pt supported carbon (PtC) catalyst in alkaline medium. Subsequently, the Co_3O_4–SP/NGr-24h catalyst has been utilized as the air electrode in a Zn–air battery, which was found to show comparable performance to the system derived from PtC. Co_3O_4–SP/NGr-24h catalyst has shown several hours of flat discharge profile at the discharge rates of 10, 20, and 50 mA/cm^2 with a specific capacity and energy density of ~590 mAh/g_{-Zn} and ~840 Wh/kg_{-Zn}, respectively, in the primary Zn–air battery system. In conjunction, Co_3O_4–SP/NGr-24h has outperformed as an air electrode in mechanical rechargeable Zn–air battery as well, which has shown consistent flat discharge profile with minimal voltage loss at a discharge rate of 50 mA/cm^2. The present results, thus demonstrate that the proper combination of the tuned morphology of Co_3O_4 with NGr will be a promising and inexpensive material for efficient and ecofriendly cathodes for Zn–air batteries.

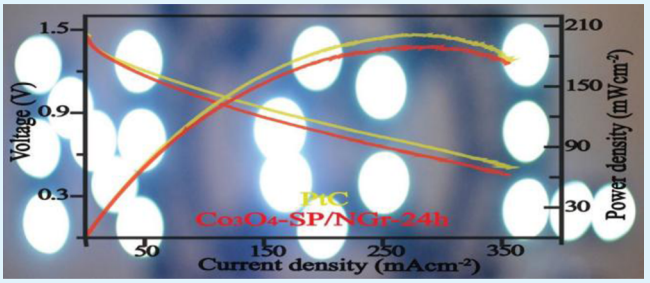

KEYWORDS: *oxygen reduction reaction, surface morphology, mixed facets, electrocatalyst, rechargeable zinc–air battery*

1. INTRODUCTION

Batteries are getting ample attention from researchers in search of renewable and sustainable energy sources. To date, Li-based batteries (Li-Bs) are the most commercialized and, of late, they are being applied to power various electronic devices and electric vehicles.[1,2] However, Li-Bs have some limitations, mainly related to their operation conditions and safety aspects.[3,4] Also, they do not satisfy the expectation of the ever increasing demand of energy and power density, mainly because of the limitations associated with their intercalation chemistry, which reduces the shelf life.[5−7] On the other hand, Zn–air battery (ZAB) is a fascinating energy generation or storage system, thanks to its high achievable specific energy, low cost, safety, and eco-friendliness due to the use of nonreactive Zn and aqueous solvents.[8−11] ZAB has been classified as a fuel cell, a primary battery, or a secondary battery, according to the technological concept or the reaction mechanism of the energy system.[12−14] However, the secondary ZABs suffer from several problems such as redistribution of Zn, formation of undesirable Zn-morphologies, formation of nonconducting ZnO layer on the anode surface, etc., which limit the lifetime of the Zn-electrode.[11,15−19] In addition, the sluggish ORR at the cathode side decreases the overall efficiency of the ZAB system.[14,20,21] Moreover, the high cost and less availability of the currently used Pt-based electrocatalysts are big challenges in front of the researchers. To overcome these issues, one of the best solutions is to make mechanical rechargeable ZAB (MR-ZAB) consisting of highly efficient non-noble-metal-based ORR electrocatalysts,[22−25] so that maximum output can be attained at a significantly reduced investment.

In that view, recently, Klaus Mullen et al.[24] demonstrated an MR-ZAB using nitrogen-doped hierarchically porous carbon as an efficient cathode material. In another work, Chen et al.[15] reported that Co_3O_4 nanowires developed on a stainless steel (SS) mesh using as a current collector displayed significant

Received: June 3, 2015
Accepted: September 10, 2015
Published: September 10, 2015

DOI: 10.1021/acsami.5b04865
ACS Appl. Mater. Interfaces 2015, 7, 21138−21149

activity in a ZAB. Similarly, Dai et al.[26] examined a CoO/CNT combined with NiFe-hydroxide as an electrocatalyst for the ZAB application. A report by Liu et al.[20] highlights the high electrocatalytic activities of hybrid MnO_2/Co_3O_4 nanoparticles for rechargeable ZABs. The same group has highlighted the rechargeable zinc−air battery fabricated with dual-phase spinel $MnCo_2O_4$ and spinel $MnCo_2O_4$/nanocarbon hybrids, which shows catalytic activity toward oxygen reduction and evolution and included a discussion on the importance of covalent interaction of the metal oxide particles with the conducting support.[27] Chen et al.[21] presented the core−corona structured LaNiO/NCNTs as an exceptional electrocatalyst for ORR and oxygen evolution reaction (OER) in rechargeable ZABs. Recently, our group investigated the bimetallic Cu−Pt nanocage structure as an efficient air electrode for primary ZAB application under pure oxygen atmosphere.[28]

From the literature review, it has been concluded that the higher activity and cost effectiveness of the ORR catalysts are the main requirements for achieving high performance and marketization of ZAB. This could be achieved by marriage of the right support substrate with a non-noble-metal-based ORR active catalyst in an effectual manner. In that line, the nitrogen-doped carbon allotropes have attracted the researchers to use as efficient metal-free electrocatalysts. The credit goes to the induced disorderness within the carbon framework due to the doped nitrogen. Mainly, the doped nitrogen transfers the electron to the neighboring carbon atom, which makes the system nonelectron-neutral.[29−33] Under these circumstances, the edge defects acquire enhanced catalytic activity compared to the graphene plane. This is assigned to the more favorable oxygen adsorption at the edge sites in comparison to the basal planes.[30,34−36]

Along with this, nonprecious metal-supported carbon-based catalysts have shown better ORR activity in comparison to their individual counterparts.[37−39] Among the family of the nonprecious metal-based catalysts, cobalt oxides (types of Co_3O_4) are considered to be champions in alkaline media.[26,37,40,41] In this case, the mixed valancies (i.e., Co^{2+} and Co^{3+}) in the fcc crystal structure of Co_3O_4 are being considered to be playing a vital role. Moreover, the main beauty of this normal spinel crystal structure, i.e., Co_3O_4, is the peculiar cation distribution in the crystal where the Co^{2+} ions reside on the 1/8th of the tetrahedral A sites while the Co^{3+} ions occupy 1/2 of the octahedral B sites.[42] This arrangement makes the system more viable for electrocatalytic applications.[25,37,43] Moreover, the surface morphology of the metal oxide and its electronic contact with the support material also play a decisive role toward the catalytic activity.[44,45] Herein, we developed a process for dispersing spherical Co_3O_4 nanoparticles on NGr and applied this easily scalable material as a non-noble metal based electrocatalyst for ORR in alkaline media. The important aspect of the present strategy is that, the hydrothermal process followed during the synthesis of the supported materials is found to be inducing time dependent morphological alteration of the Co_3O_4 nanoparticles, and reaction duration of 24 h is found to be producing spherical nanoparticles of Co_3O_4 with relatively high roughness factor. Concomitantly, NGr acts as the support material by ensuring an even distribution of the Co_3O_4 nanoparticles. Here, the doped nitrogen of NGr is found to be playing a dual role by acting as an efficient nucleating site and also by assisting in controlling the growth kinetics of the Co_3O_4 nanoparticles.[46,47] The tuning of the structural growth pattern of the Co_3O_4 nanoparticles and the associated synergistic interactions existing within the system are found to be significantly helping the supported material to acquire an ability to reduce molecular oxygen at a significantly reduced overpotential.[48] Considering this advantage of the material, the prepared catalyst has been investigated toward ORR in the primary and mechanically rechargeable ZAB and is found to be highly active and durable under the operating conditions.

2. EXPERIMENTAL SECTION

Materials. Cobalt acetate, zinc foil, graphite powder, phosphoric acid (H_3PO_4), potassium hydroxide (KOH), sulfuric acid (H_2SO_4), potassium permanganate ($KMnO_4$), and melamine were procured from Sigma-Aldrich. Hydrogen peroxide (H_2O_2), ethanol (EtOH), and hydrochloric acid (HCl) were purchased from Thomas Baker. All the chemicals were used as such without any post treatment. Carbon paper was procured from Toray, Japan.

Synthesis of Graphene Oxide (GO). Improved Hummer's method was used for the GO synthesis.[49] In brevity, graphite and $KMnO_4$ were mixed well in the ratio of 1:6. Subsequently, the above mixture was added slowly and carefully into a mixed solution of H_3PO_4:H_2SO_4 (1:9). The reaction mixture (RM) was subjected to heating for 24 h (60 °C), after the complete addition. Consequently, the obtained RM was slowly quenched into ice having 3% H_2O_2 solution. The yellow solution obtained was centrifuged and consequently washed with deionized water. Later, the product was washed with 30% HCl solution to get ride-off the metal impurities. Finally, the obtained dark chocolate colored product was washed with ethanol and acetone followed by diethyl ether and was kept for drying in open atmosphere.

Synthesis of Reduced Graphene Oxide (Gr). The reduced graphene oxide was synthesized by thermal reduction of GO. 500 mg of GO was kept in a tube furnace under argon environment and temperature of the furnace was increased to 800 °C while maintaining a temperature ramp of 5 °C/min. The temperature of the furnace was kept constant at 800 °C for 2 h. The obtained fluffy black colored product was collected and is termed as Gr.

Synthesis of N-Doped Graphene (NGr). GO and melamine were mixed in the ratio of 1:5 and this mixture was subsequently dispersed in 100 mL of DI water by ultrasonication for 10 min. The obtained mixture was kept on stirring for 24 h. The temperature of the magnetic stirrer was maintained at 80 °C to get a dried uniform mixture of GO and melamine. The obtained powder was calcined at about 800 °C in an Ar atmosphere for 4 h. Finally the furnace was cooled to room temperature in the same environment and a black colored powder was collected, which is termed as NGr.

Synthesis of Co_3O_4-Supported NGr Catalysts. Sixty and forty milligrams of cobalt acetate and NGr, respectively, were dispersed well in a 3:2 mixture of ethanol and water by subjecting it for probe ultrasonication for 30 min. Later, the above mixture was transferred into a Teflon coated SS-autoclave (50 mL) and was kept in an oven at 120 °C for different time intervals (9, 12, 24, and 48 h). Finally, the obtained product in each case was filtered and washed with DI water. The materials thus collected were dried at 80 °C (for 10 h) in an oven. The samples obtained corresponding to the time intervals of 9, 12, 24, and 48 h are designated as Co_3O_4−NC/NGr-9h, Co_3O_4−BC/NGr-12h, Co_3O_4−SP/NGr-24 and Co_3O_4/NGr-48h, respectively. Here, NC, BC, and SP stand for nano cubes, blunt cubes and spherical particles, respectively, which represent the shape of the Co_3O_4 nanoparticles formed on the surface of NGr in each case.

Synthesis of Co_3O_4-Supported Gr Catalyst. For the purpose of comparing the influential role of nitrogen doping on Gr, along with the previously mentioned NGr based samples, we have also prepared the Co_3O_4 supported Gr sample by following the similar protocol used for the synthesis of Co_3O_4−SP/NGr-24. Here, instead of NGr, Gr was used as the support during the process. The obtained product is named as Co_3O_4/Gr-24h.

Zinc−Air Battery Fabrication and Testing. ZAB was tested in home-built electrochemical cells using Zn-foil and Co_3O_4−SP/NGr-24h as the anode and cathode electrodes, respectively. The cathode

DOI: 10.1021/acsami.5b04865
ACS Appl. Mater. Interfaces 2015, 7, 21138−21149

electrode was fabricated by using Co_3O_4–SP/NGr-24h. Before that, the catalyst slurry was prepared by sonicating Co_3O_4–SP/NGr-24h in isopropyl alcohol for 1 h. Later, 10 wt % Nafion solution was added into the above sonicated solution and the mixture was kept for further sonication of 1 h. The resulting catalyst slurry was brush coated on a Toray carbon paper (GDL) and dried at 60 °C for 1 h to achieve a catalyst loading of 1.0 mg/cm^2 (electrode area = 1.0 cm^2). Moreover, a rough surface-polished zinc foil was used as an anode of the same area. Finally, ZAB was fabricated by pairing the Zn-foil and Co_3O_4–SP/NGr-24h electrodes in 6.0 M KOH using the Celgard membrane as a separator. Afterward, this fabricated ZAB setup was tested at room temperature by using galvanodynamic experiment with a multichannel VMP-3 model Bio-Logic potentiostat. The steady-state polarization of the assembled ZAB setup was tested at 5 mV/s. The galvanostatic discharge curves of ZABs were recorded at different current densities, mainly 10, 20, and 50 mA/cm^2.

Material Characterization. The sample preparation for high-resolution transmission electron microscopy (HR-TEM) analysis was done by making dispersed solution of the catalysts (1 mg) in isopropyl alcohol (5 mL). The dispersed solution was drop-casted on a carbon coated Cu grid and, after drying under a lamp, it was used for the imaging purpose. All the TEM images were recorded by using FEI, TECNAI G2 F20 instrument (accelerated voltage = 300 kV, Cs = 0.6 mm, resolution = 1.7 Å. For the recoding of X-ray diffraction (XRD) patterns, Rigaku Smartlab diffractometer for Cu Kα radiation (λ = 1.5406 Å), at a scan rate of 2° min^{-1} was used. Thermogravimetric analysis (TGA) was accomplished by using a SDTQ600 TG-DTA Instruments. All the TGA analyses were completed under oxygen environment by maintaining a temperature ramp of 10 °C/min. X-ray photoelectron spectroscopy (XPS) analysis was carried out by using VG Microtech Multilab ESCA 3000 spectrometer. The XPS system was equipped with an Mg Kα- X-ray source ($h\nu$ = 1.2536 keV). For the Raman analysis of the samples, an HR 800 Raman spectrometer (Jobin Yvon, Horiba, France) with a 632 nm red laser (NRS 1500 W) was used.

Electrochemical Characterization. The electrochemical investigation has been done on a Bio-Logic potentiostat (model VMP-3) using cyclic voltammetry (CV), linear sweep voltammetry (LSV), and rotating ring disc electrode (RRDE) (Pine Instruments) techniques. The test cell involves a three-electrode system. The catalyst-coated glassy carbon electrode (GCE) was used as the working electrode, mercury/mercury oxide (Hg/HgO) as the reference electrode and a platinum flag as the counter electrode. Moreover, the catalyst ink was prepared by mixing the catalyst (5 mg) and 40 μL of 5% w/v Nafion in 1 mL of aqueous solution of ethanol (ethanol:water is 3:2) for 1 h. A 10 μL of the above prepared catalyst ink was drop-casted on the surface of GCE. Prior to use, GCE was polished with aqueous alumina slurry (size: 0.3 and 0.5 μm). The catalyst coated GCE was subsequently dried at room temperature and was used as the working electrode for all the further electrochemical investigations. An aq. 0.1 M KOH was used as the electrolyte for CV, RDE, and RRDE studies. For the ZAB testing, a 6 M KOH solution was used as the electrolyte.

3. RESULTS AND DISCUSSION

Scheme 1 depicts the synthesis methodology adopted for preparing the Co_3O_4 supported NGr catalysts by using the hydrothermal method and the application of the best catalyst derived in the series for the development of MR-ZAB. Co_3O_4 supported NGr is found to be giving different morphologies of Co_3O_4 by varying the reaction time, all the while keeping the reaction temperature constant. The morphology acquired by the Co_3O_4 nanoparticles in each case could be confirmed through the TEM analysis. Figures 1a and 2j, k show well-defined dispersion of spherical nanoparticles of Co_3O_4 (Co_3O_4–SP) on NGr in the case of Co_3O_4–SP/NGr-24, with the particle size falling approximately to 60 nm. However, contrary to the NGr-based system, in the case of the Gr-supported system, i.e., Co_3O_4/Gr-24h, the dispersion of Co_3O_4

Scheme 1. Synthesis of Different Morphologies of Co_3O_4 Supported NGr Catalysts by Varying the Reaction Time in the Hydrothermal Process; Application of the Developed Co_3O_4–SP/NGr-24h Catalyst As an Air Electrode for Primary and Mechanically Rechargeable ZAB Has Been Demonstrated in This Manuscript

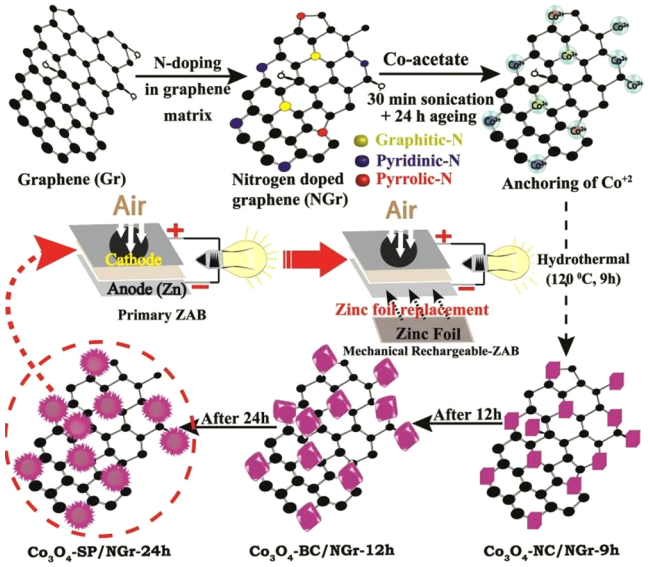

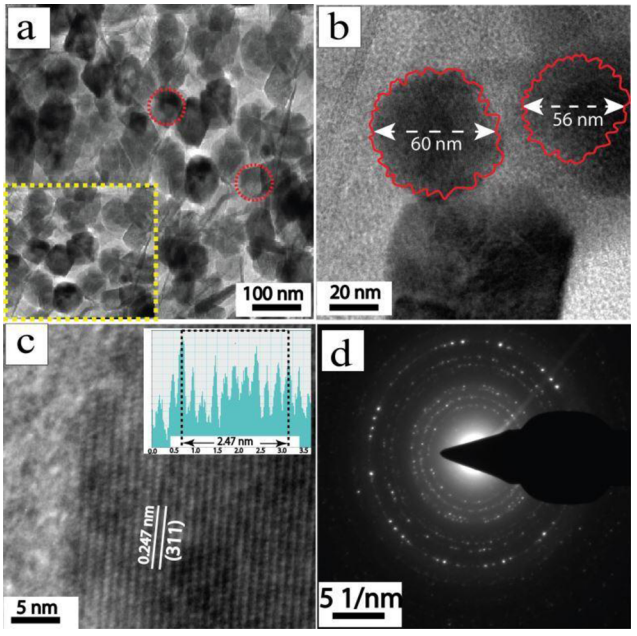

Figure 1. TEM images of Co_3O_4–SP/NGr-24h: (a) good dispersion of the Co_3O_4 spherical nanoparticles supported on NGr, (inset: exposed spherical Co_3O_4 particles), (b) Co_3O_4–SP/NGr-24h with spherical edges, where the red colored margin indicates the surface roughness of the Co_3O_4 nanoparticle, (c) HR-TEM image with lattice fringes (inset: lattice profile), and (d) SAED pattern of Co_3O_4–SP/NGr-24h.

is found to be very poor (Figure 2a). The change in the behavior of the Co_3O_4 nanoparticles on Gr and NGr in terms of their dispersion is mainly assigned to the effective bonding between the nitrogen of NGr and the Co_3O_4 nanoparticles. Mainly, the doped nitrogen creates additional anchoring sites which facilitate the dispersion of the Co_3O_4 nanoparticles. In

DOI: 10.1021/acsami.5b04865
ACS Appl. Mater. Interfaces 2015, 7, 21138–21149

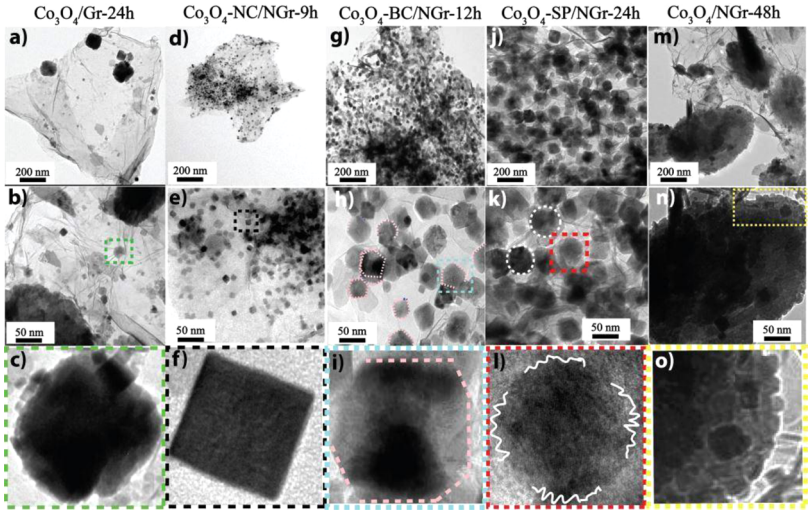

Figure 2. TEM images of the Co_3O_4 nanoparticles supported Gr/NGr electrocatalysts synthesized at different reaction time intervals. (a, b) Dispersion of Co_3O_4 nanoparticles on the Gr support (i.e., Co_3O_4/Gr-24h), (c) enlarged view of image b marked with the green colored dotted line, (d, e) dispersion of Co_3O_4 nanocubes on the NGr support (i.e., Co_3O_4−NC/NGr-9h), (f) enlarged view of image e marked with the black colored dotted line, (g, h) dispersion of Co_3O_4 blunt edge cubes on the NGr support (i.e., Co_3O_4−BC/NGr-12h), (i) enlarged view of image h marked with the cyan colored dotted line, (j, k) dispersion of Co_3O_4 spherical nanoparticles on the NGr support (i.e., Co_3O_4−SP/NGr-24h), (l) enlarged view of image k marked with the red colored dotted line (rough surface of Co_3O_4−SP is marked with the white colored line), (m, n) agglomeration of the Co_3O_4 particles on the NGr support (i.e., Co_3O_4/NGr-48h), and (o) enlarged view of image n marked with the yellow colored dotted line.

addition to the dispersion, the doped nitrogen is also found to be playing as an influential entity in controlling the size distribution (Figure S1) of the Co_3O_4 nanoparticles on NGr. Among the various NGr samples prepared, the particle size of Co_3O_4 is also found to be strongly influenced by the duration of the hydrothermal reaction. Accordingly, the particle size of the homemade catalysts is found to be following the order of Co_3O_4 /NGr-48h (∼150 ± 30 nm) > Co_3O_4−SP/NGr-24h (∼60 ± 3 nm) > Co_3O_4−BC/NGr-12h (∼50 ± 3 nm) > Co_3O_4−NC/NGr-9h (∼40 ± 3 nm). Mainly, the size of Co_3O_4 on NGr is found to be increased from 40 to 150 nm, when the reaction time increased from 9 to 48 h (Figure 2d−o and Figure S1). Moreover, the Co_3O_4 dispersion on the non-nitrogen-doped graphene (Gr) (Co_3O_4/Gr-24h) was found to be inconsistent in size and distribution in comparison to the NGr supported systems (Figure 2a−c). Along with the size variation, the amount of Co_3O_4 on NGr is also being varied with the reaction time (Figure S2). It seems to be the 9 h reaction time duration is not enough to achieve the complete dispersion of Co_3O_4 nanoparticles. Therefore, the major difference in the acquired sizes of Co_3O_4 on NGr (Co_3O_4−SP/NGr-24h) and Gr (Co_3O_4/Gr-24h), where the reaction time was set as 24 h in both the cases, highlights the significance of nitrogen doping in carbon network in achieving proper dispersion of the Co_3O_4 nanoparticles even though they are prepared under similar experimental conditions.

Interestingly, we found that as the time of the reaction increased, the edges of Co_3O_4−NC started to become blunt before its agglomeration (Figure 2d−o). This can be visualized from the transformation of the perfect cubical morphology of Co_3O_4 in the case of Co_3O_4−NC/NGr-9h (Figure 2d−f) to blunt edged cubes in the case of Co_3O_4−BC/NGr-12h (Figure 2g−i) and thereafter to rough edged spherical particles in the case of Co_3O_4−SP/NGr-24h (Figure 2j−l). This could be assigned to the transformation of the higher to the lower surface energy plane crystal structure. This structural transformation is expected to lead to the formation of the mixed facets of the exposed Co-oxide crystals. Among the homemade samples, Co_3O_4−SP/NGr-24h has shown the dominance of the exposed (311) plane (marked in Figures 1c, d and 2l and Figure S3). This has been confirmed from the lattice profile analysis, where the calculated value of the *d*-spacing of Co_3O_4−SP/NGr-24h is found to be 0.247 nm, which is assigned to the (311) planes of Co_3O_4−SP (Figure 1c, inset).[50−52] Fascinatingly, a close inspection of the HR-TEM images of Co_3O_4−SP/NGr-24h shown in Figures 1b and 2l reveal that the surface of Co_3O_4 nanoparticle is not uniform. It is found to have acquired a rough surface morphology that might improve the surface area and roughness factor in comparison to the all the other prepared catalysts. Details about the surface area and roughness factor calculation have been given in a later section of this manuscript. In addition, the selected area electron diffraction (SAED) pattern confirms the crystallinity of the particles (Figure 1d). To acquire a more clear understanding of the crystal structure transformation, we took the images of the 48 h reaction sample, which is found to be an agglomeration of the Co_3O_4 nanoparticles (Figure 2m, n). The average particle size of Co_3O_4/NGr-48h sample is measured to be around 150 ± 30 nm (Figure S1). This transformation in the morphology of Co_3O_4 might be due to the overgrowth of the Co_3O_4 crystals with the increasing reaction time (Figure 2m, n).

Furthermore, X-ray diffraction (XRD) technique was used to understand the phase of Co_3O_4 and change in diffraction peaks during the structural transformation (Figure 3). The XRD analysis has been done in the range of 2θ from 10 to 80°. The XRD spectra (Figure 3) show a good crystalline structure of Co_3O_4 as verified by the well-defined sharp diffraction peaks corresponding to the (111), (200), (220), (311), and (222) crystal facets from the Co_3O_4 particles. The XRD result indicates that the present cobalt oxide is in the form of normal spinel possessing the fcc crystal structure.[53] The observed diffraction peaks namely (111), (220), (311), (222), (400), (511), and (440) at the 2θ values of 19.84, 31.21, 36.66, 38.91, 42.13, 59.52, and 65.29°, respectively, are indicating the spinel

DOI: 10.1021/acsami.5b04865
ACS Appl. Mater. Interfaces 2015, 7, 21138−21149

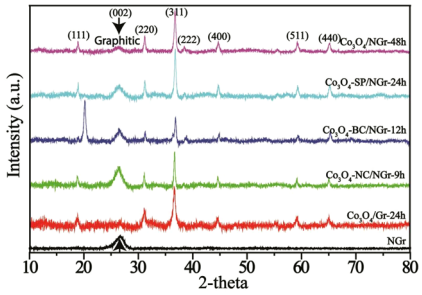

Figure 3. Comparative X-ray diffraction patterns of NGr, Co_3O_4/Gr-24h, Co_3O_4–NC/NGr-9h, Co_3O_4–BC/NGr-12h, Co_3O_4–SP/NGr-24h, and Co_3O_4/NGr-48h. The black colored arrow indicates the position of the graphitic (002) plane.

characteristics of Co_3O_4.[44] The calculated *d*-spacing value from the (311) peak is found to be ∼0.249 nm, which matches well with the *d*-spacing value derived from the HR-TEM results (Figure 1c and Figure S3). Furthermore, the peak at ∼26.39° is assigned to the G (002) plane of NGr.[54,55] Importantly, the relative intensity of the (311) plane of Co_3O_4 is clearly found to be gradually increasing as the reaction time goes to 24 h, which clearly highlights the improved exposure of the (311) crystal plane under the synthetic conditions.[56,57] In addition, to confirm the same, we have calculated the texture coefficient (TC) for the diffraction peaks observed in case of Co_3O_4–SP/NGr-24h, which is found to be greater than unity for (311) and less than unity for all the other peaks.[57] The TC has been calculated by using the formula given in eq 1.[57]

$$TC(hkl) = \frac{\frac{I(hkl)_i}{I_o(hkl)_i}}{\frac{1}{N}\sum_{i=1}^{n}\frac{I(hkl)_i}{I_o(hkl)_i}} \quad (1)$$

where $I(hkl)$ = observed intensity of the (hkl) plane of Co_3O_4–SP/NGr-24h, $I_0(hkl)$ = intensity of the (hkl) plane reported in reference (JCPDS card no. 80–1545). N = total number of reflections taken into account.

This highlights the (311) crystal plane is more exposed in the Co_3O_4–SP/NGr-24h. It should be noted that the relative peak intensity of the (311) plane is found to be decreased for Co_3O_4/NGr-48h (Figure 3). This could originate from the time-dependent intrastructural modifications affected on the Co_3O_4 nanoparticles, which lead to the transformation of the cubical forms of the particles to the spherical forms as the reaction time reaches to 48 h. This has been substantiated by the TEM images (Figure 2d–i) of the sample, which indicate the presence of spherical Co_3O_4 particles on the NGr surface.

Furthermore, to confirm the extent of loading of Co_3O_4 and stability of the supported catalysts, TGA has been performed, where the samples were scanned in the temperature range of 25–800 °C with a scan rate of 10 °C/min in an oxygen atmosphere. Figure S2, provides the comparative TGA curves of NGr, Co_3O_4/Gr-24h, Co_3O_4–NC/NGr-9h, Co_3O_4–BC/NGr-12h, Co_3O_4–SP/NGr-24h, and Co_3O_4/NGr-48h. In all the cases, the initial weight loss at ∼100 °C is assigned to the loss of physisorbed water molecules and the weight loss between 350 and 750 °C is assigned to the burning of carbon. TGA curves of Co_3O_4/Gr-24h, Co_3O_4–NC/NGr-9h, Co_3O_4–BC/NGr-12h, Co_3O_4–SP/NGr-24h and Co_3O_4/NGr-48h show a final weight of 19.61, 19.88, 23.90, 33.17, and 35.13%, respectively, indicating the corresponding loading of the cobalt oxide in the prepared samples. The cobalt oxide loading is found to be different in all the samples and this indicates the relationship with the reaction time and the nature of the support substrate. The Gr supported sample (Co_3O_4/Gr-24h) shows lesser % of Co_3O_4 in comparison to that of the NGr supported sample (Co_3O_4–SP/NGr-24h), even though both the catalysts are prepared under the similar reaction conditions. From the TGA data, it can be clearly seen that the doped nitrogen is playing a very important role toward the anchoring of the Co_3O_4 nanoparticles and increasing the stability of the overall catalyst in comparison to the Gr supported catalyst. This could be assigned to the intimate contact between the doped nitrogen of NGr and Co_3O_4 particles. Moreover, the effective-interaction of the present nitrogen of NGr and Co_3O_4 influences the basic electronic structure of Co_3O_4, which eventually helps during the electrocatalytic application of the material.

To understand the exact local electronic and chemical configuration of the Co_3O_4 nanoparticles supported on Gr/NGr, we have carried out XPS analysis (Figure 4 and Figure

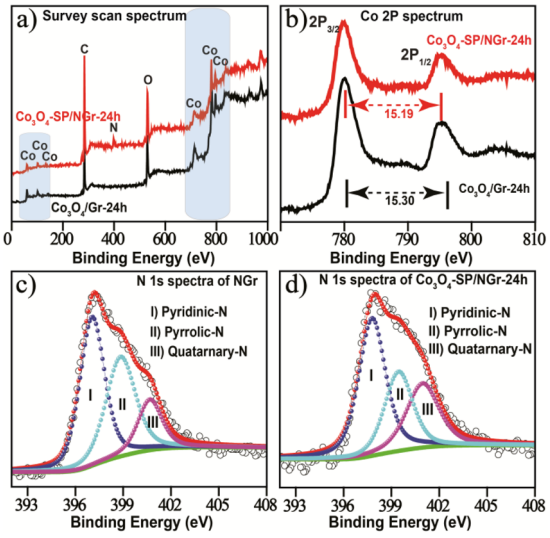

Figure 4. Comparative XPS: (a) survey scan and (b) Co 2p spectrum of Co_3O_4/Gr-24h and Co_3O_4–SP/NGr-24h. Deconvoluted N 1s spectra of (c) NGr and (d) Co_3O_4–SP/NGr-24h.

S4). The N 1s spectra of NGr (Figure 4c) and Co_3O_4–SP/NGr-24 (Figure 4d) have been deconvoluted into three subpeaks in each case. In the case of NGr, these peaks are appeared at 398.61 ± 0.30, 400.48 ± 0.30, and 402.84 ± 0.30 eV, which are identified as the signatures corresponding to the pyridinic-N, pyrrolic-N, and quaternary-N, respectively.[54,55] On the other hand, the corresponding peaks in the case of the deconvoluted N 1s spectra of Co_3O_4–SP/NGr-24 are appeared at 397.2, 399.45, and 401.86 eV. Interestingly, the lower binding energy shift by ∼1.0 eV of all the N 1s subpeaks of Co_3O_4–SP/NGr-24h, in comparison to the corresponding subpeaks of NGr (N 1s), indicates the effectual bonding between Co_3O_4–SP and the doped nitrogen of NGr and this ascertains to the involvement of the transfer of electron between the Co-oxide and NGr. This mutual electron transfer is responsible for the shifting of the binding energy (lower shift) of the N 1s of Co_3O_4–SP/NGr-24h in comparison to that of NGr.[47,48] This is also authenticated from the different electronegativity of nitrogen (3.0) and cobalt (1.8).[58,59]

DOI: 10.1021/acsami.5b04865
ACS Appl. Mater. Interfaces 2015, 7, 21138–21149

Furthermore, from the XPS spectra given in Figure 4c, d, the nitrogen percentage in NGr and Co_3O_4−SP/NGr-24h is calculated, which is found to be 3.8 wt % in both the cases. Moreover, the Co 2p spectra shows two main peaks at 780.50 and 795.80 eV, which are assigned to the Co $2p_{3/2}$ and $2p_{1/2}$, respectively, with a characteristic peak difference of ∼16.00 eV. In addition to this, the trivial shift in the binding energy of Co 2p of Co_3O_4−SP/NGr-24h in comparison to Co_3O_4/Gr-24h could be associated with the movement of electron between the nitrogen of NGr and Co-oxide. This might help to strengthen the bonding between the entities.

The comparative Raman spectra of Gr, NGr, Co_3O_4/Gr-24h, and Co_3O_4−SP/NGr-24h (Figure 5) show two prominent

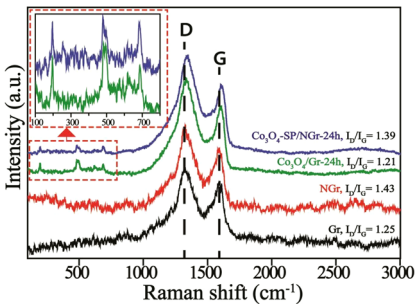

Figure 5. Comparative Raman spectra of Gr, NGr, Co_3O_4/Gr-24h, and Co_3O_4−SP/NGr-24h samples (Inset: exposed Co_3O_4 band, corresponding to the low energy vibrational peaks).

peaks at ∼1326.00 and ∼1588.00 cm^{-1}, which could be assigned to the D-band and G-band of the carbon material.[49,54] The D stands for the defects and G stands for graphitic.[42,45] The G-band peak at 1588 cm^{-1} is due to the in plane bond stretching of C═C, which is strongly coupled in the hexagonal sheets of graphene. Along with the D- and G-band peaks of the carbon, additional peaks in the range of 150−750 cm^{-1} are observed which could be assigned to the longitudinal and transverse optical phonon mode vibration peaks of the Co_3O_4 nanoparticles supported Gr/NGr samples.[44,60] This represents the vibration mode of the graphitic lattice with the E_{2g} symmetry, which is an indication of the highly ordered graphitic carbon materials.[54] The intensity ratio of the D and G-band (I_D/I_G) gives information about the average size of the sp^2 domains with the degree of disorderness. The increased I_D/I_G ratio from 1.25 to 1.43 for Gr and NGr, respectively, provides the evidence of higher degree of defects after the nitrogen doping. However, the I_D/I_G ratio slightly decreases from 1.25 to 1.21 after the Co_3O_4 decoration on the Gr (Co_3O_4/Gr-24h) support. Similarly, in the case of the NGr supported Co_3O_4 sample (Co_3O_4−SP/NGr-24h), the I_D/I_G ratio is found to be decreased from 1.43 to 1.39. This observed trend could be attributed to the restoring of the graphene structure to some extent upon the Co_3O_4 loading.[61] It is also evident that in comparison to pristine NGr at the same region, the D and G peaks of the Raman spectrum of Co_3O_4−SP/NGr-24h show obvious peak shift toward higher wavenumber (cm^{-1}). This shift in the spectra is mainly because of two factors; one is the carrier density modulation induced by the charge transfer and the other is the introduction of the mechanical strain by the supported metals.[62−67]

To investigate the effect of the modulated properties of the Co_3O_4 supported Gr/NGr samples and their structural transformation with the reaction time, electrochemical performance has been screened by CV, RDE, and RRDE studies. Mainly, the prepared electrocatalysts have been screened for ORR in 0.1 M KOH solution by keeping a constant mass loading (0.05 mg) on a GCE. The commercial PtC has been used for the comparison study.

The CV measurements in O_2-saturated 0.1 M KOH showed that the onset potential afforded by Co_3O_4−SP/NGr-24h (0.03 V versus Hg/HgO) catalyst is lower than that of PtC (0.10 V), but higher in comparison to the other prepared samples (−0.10, −0.30, and −0.16 V for NGr, Co_3O_4 and Co_3O_4/Gr-24h, respectively) (Figure S5). Furthermore, to clearly understand the intrinsic electrocatalytic activity, RDE studies of the different catalysts have been performed (Figure S6). Specifically, the comparative linear sweep voltammograms (LSVs) of Co_3O_4−SP/NGr-24h, Co_3O_4/Gr-24h, Co_3O_4, NGr and PtC recorded at 1600 rpm (scan rate: 10 mV/s) are shown in Figure 6a. It can be seen that Co_3O_4−SP/NGr-24h has

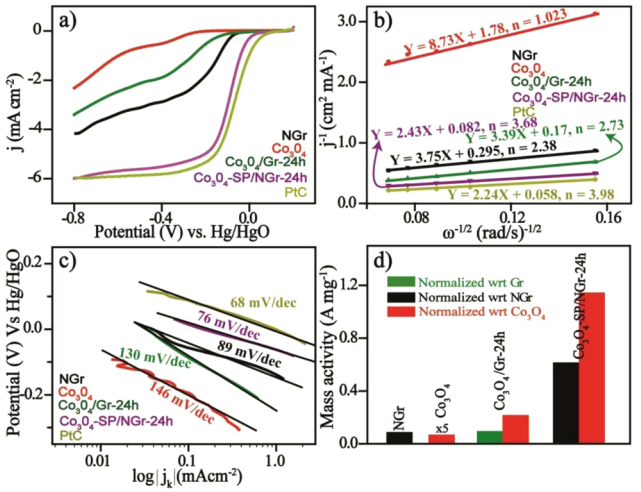

Figure 6. ORR performance of Co_3O_4−SP/NGr-24h and reference catalysts: (a) ORR polarization plots of Co_3O_4−SP/NGr-24h and the reference catalysts at 1600 rpm of the disc electrode in 0.1 M KOH solution (the mass loading of catalysts was kept constant to 0.05 mg), (b) Koutecky−Levich plots at −0.60 V (vs. Hg/HgO), (c) comparative Tafel plots of NGr, Co_3O_4, Co_3O_4/Gr-24h, Co_3O_4−SP/NGr-24h and PtC catalysts, and (d) mass activity of the catalysts @ 0.0 V (vs. Hg/HgO) after normalizing with the mass of Co_3O_4 and support material, separately.

shown superior activity in comparison to Co_3O_4/Gr-24h, Co_3O_4, and NGr (Figure 6a). It should be noted that a well-featured LSV profile could be obtained in the case of Co_3O_4−SP/NGr-24h with a close matching performance characteristics as that of the state-of-the-art PtC catalyst. The onset potential for ORR in the case of Co_3O_4−SP/NGr-24h is 0.03 V, which indicates that the overpotential experienced by the present system over its Pt counterpart is only 70 mV. The half-wave potential ($E_{1/2}$), which is an indication of how well the system performs under a demand of current, of Co_3O_4−SP/NGr-24h (−0.11 V) is also found to be very close to the $E_{1/2}$ of PtC (−0.07 V). The comparative $E_{1/2}$ values of all the prepared catalysts are given in Table S1. This can be taken as a valid indication on the high number density of the active sites acquired along the surface of NGr. On the other hand, the activity of Co_3O_4/Gr-24h is found to be significantly low in comparison to Co_3O_4−SP/NGr-24h and this could be assigned to the reasons like the lower surface-to-volume ratio, the weak

DOI: 10.1021/acsami.5b04865
ACS Appl. Mater. Interfaces 2015, 7, 21138−21149

interaction of Co_3O_4 with Gr and the nonuniform distribution of Co_3O_4 particles on Gr. All of these can be featured enough to cause a low density exposure of the active sites in the case of Co_3O_4/Gr-24h, which concurrently attracts a big penalty in terms of both the onset potential and $E_{1/2}$ as can be observed from the LSV profile of the sample (Figure 6a).

Despite the advantages obtained in the case of Co_3O_4–SP/NGr-24h, the similar Co_3O_4-supported NGr systems prepared at the lower as well as at very higher reaction time durations, i.e., Co_3O_4–NC/NGr-9h, Co_3O_4–BC/NGr-12h, and Co_3O_4/NGr-48h, are found to be showing very high overpotential and lower limiting current in comparison to Co_3O_4–SP/NGr-24h (shown in Figure S6). The lower ORR activity of Co_3O_4–NC/NGr-9h and Co_3O_4–BC/NGr-12h might be assigned to the structural variation along with the surface modification (shown in Figure 2f, i). As mentioned earlier, Co_3O_4 displayed cubical as well as blunt-edged cubical structures in Co_3O_4–NC/NGr-9h and Co_3O_4–BC/NGr-12h, respectively, which possess different exposed crystal planes and other surface characteristics (Figures 2d–i and 3). Contrary to these two cases, Co_3O_4–SP/NGr-24h possesses superior activity in comparison to the rest of the homemade samples, which could be due to the presence of the rough surface and spherical morphology (Figure 2l) of the Co_3O_4 nanoparticles. It should be noted that this activity modulation toward ORR has been accomplished solely through the structural changes induced on the Co_3O_4 nanoparticles when the duration of the hydrothermal process elapse a limit to attain the conversion of the oxide particles from cubical to spherical.[45,68] However, in the case of Co_3O_4/NGr-48h, which also has spherical Co_3O_4 particles, the performance is found to be inferior to its 24 h counterpart. Here, in the former case, the particles get agglomerated because of the higher reaction time involved in the synthesis, which results in a lower surface-to-volume ratio (lower specific surface area). Despite this, we found smaller Co_3O_4 particle size (higher specific surface area) for Co_3O_4–NC/NGr-9h and Co_3O_4–BC/NGr-12h in comparison to Co_3O_4–SP/NGr-24h. However, regardless of the smaller size of the former two samples, the electrochemical activity is found to be better for Co_3O_4–SP/NGr-24h. Therefore, the higher activity of Co_3O_4–SP/NGr-24h is mainly credited to the higher electrochemical surface area and roughness factor originated from the uneven/rough surface of the Co_3O_4 nanoparticles (Figure 2l). The electrochemical surface area (ECSA) has been calculated by recording the noncapacitive CV with different scan rates in a potential window of 0.1 V in the range of ±0.05 V from the open circuit potential (OCP) (Figure S7).[69] Subsequently, the slopes of the anodic and cathodic currents at OCP give the value of the electrical double layer capacitance (C_{dl}). The the ratio of C_{dl} to the specific capacitance (Cs), subsequently, gives the ECSA.[70] The calculated ECSA follows the order of Co_3O_4–SP/NGr-24h (16.29 cm^2) > Co_3O_4–BC/NGr-12h (9.25 cm^2) > Co_3O_4–NC/NGr-9h (8.58 cm^2) > Co_3O_4/NGr-48h (7.77 cm^2). Furthermore, the roughness factor (RF) has been calculated from the ratio of ECSA to the geometrical area of the glassy carbon electrode (GCE, 0.19625 cm^2). The obtained RF is found to be higher for Co_3O_4–SP/NGr-24h (83.0) in comparison to Co_3O_4–BC/NGr-12h (47.1), Co_3O_4–NC/NGr-9h (43.7), and Co_3O_4/NGr-48h (39.59). In short, it can be seen that the ECSA, RF, and morphology of Co_3O_4 are contributing significantly by bringing a direct impact on the electrochemical activity.

To acquire further understanding on the reaction kinetics, we have recorded the LSVs of Co_3O_4–SP/NGr-24h at different rotation rates of the working electrode (Figure S8) and investigated the kinetics of ORR with the help of Koutecky–Levich (K–L) equations.[28] The current density is found to be increased with increasing the rotation rate, which could be assigned to the better mass transport to the electrode surface (Figure S8). The obtained current density (j) at different rotation rates of the working electrode can be expressed by the K–L equation for investigating the kinetics of ORR (details are given in the Supporting Information). Figure 6b shows the K–L plots ($j^{-1/2}$ versus $\omega^{-1/2}$) at −0.60 V (vs. Hg/HgO), where the number of electron transferred per oxygen molecule (n) reduction can be obtained from the slope of the plots. The calculated *n*-value obtained for Co_3O_4–SP/NGr-24h electrode is 3.7, which represents a major contribution by the 4-electron ($4e^-$) transfer mechanism as normally found in the case of PtC (Figure 6b). From the K–L plots, the kinetic current density values calculated for the prepared electrocatalysts are found to be following the order of PtC (17.24 mA/cm^2) > Co_3O_4–SP/NGr-24h (12.19 mA/cm^2) > Co_3O_4/Gr-24h (5.88 mA/cm^2) > NGr (3.38 mA/cm^2) > Co_3O_4 (0.5617 mA/cm^2). Because the kinetic current density is generally being taken as a strong indicator to quantify the intrinsic activity of the catalysts, the above results unambiguously confirm the superior activity of Co_3O_4–SP/NGr-24h in comparison to the rest of the prepared samples. From the aforementioned discussions, it can be seen that in the case of Co_3O_4–SP/NGr-24h, multiple factors work in favor of it to tune it out as a catalyst with modulated activity characteristics toward ORR. The coordination of the nitrogen functionalities with Co_3O_4, the higher ECSA and RF acquired because of the surface restructuring of Co_3O_4 and the homogeneous particle dispersion accomplished in the system are the vital factors that induced a controlled interplay to attain the desired property modulation in the case of Co_3O_4–SP/NGr-24h. Similarly, the poor activity of the Co_3O_4 and Co_3O_4-supported graphene systems could be ascribed to the presence of less functionality on Gr, weak interaction between the Co-oxide particles and the support substrate, lesser active sites, lower ECSA, and poor RF.

It is well-known that the rate of transfer of electron, i.e., kinetics involved in ORR, is another important parameter relevant to the activity of the catalysts that can be understood from the Tafel plot. Co_3O_4–SP/NGr-24h has shown a Tafel slope of ∼76 mV per decade at lower current density, which augments nearly comparable activity of Co_3O_4–SP/NGr-24h to PtC (Figure 6c). As a standard, the commercial PtC has also been tested, which displays a Tafel slope of ∼68 mV per decade. Overall, the order of Tafel slope of the prepared samples is PtC (68 mV per decade) < Co_3O_4–SP/NGr-24 h (76 mV per decade) < NGr (89 mV per decade) Co_3O_4/Gr-24 h (130 mV per decade) < Co_3O_4 (146 mV per decade). Therefore, such a lower Tafel slop of Co_3O_4–SP/NGr-24h compared to the rest of the systems indicates that ORR is more favorable on the surface of Co_3O_4–SP/NGr-24h.[71,72] Furthermore, to understand the quality of the electrocatalyst, mass activity has been calculated at 0.0 V (vs. Hg/HgO). Figure 6d provides the comparative mass activity of NGr, Co_3O_4, Co_3O_4/Gr-24h, and Co_3O_4–SP/NGr-24h. The current at 0.0 V vs Hg/HgO has been normalized with respect to the mass of Co_3O_4 and NGr, separately (Figure 6d). Co_3O_4–SP/NGr-24h is showing higher mass activity (1.14 A/mg_{-Co3O4} and 0.62 A/mg_{-NGr}) in comparison to Co_3O_4/Gr-24h (0.21 A/mg_{-Co3O4}

DOI: 10.1021/acsami.5b04865
ACS Appl. Mater. Interfaces 2015, 7, 21138–21149

and 0.10 A/mg$_{-Gr}$) at 0.0 V (vs Hg/HgO) (Figure 6d). Looking it very closely, Co_3O_4−SP/NGr-24h is found to be showing ∼5.4 and ∼6.0 times improved mass activity in comparison to Co_3O_4 and Gr/NGr, respectively. Again, this improved mass activity of Co_3O_4−SP/NGr-24 h could be attributed to the structure, higher ECSA, and RF associated with the system.

Furthermore, to understand the ORR pathways of the prepared materials, the peroxide species (HO_2^-) formation during the ORR process was examined by RRDE measurements (shown in Figure 7 and Figure S9). In case the system

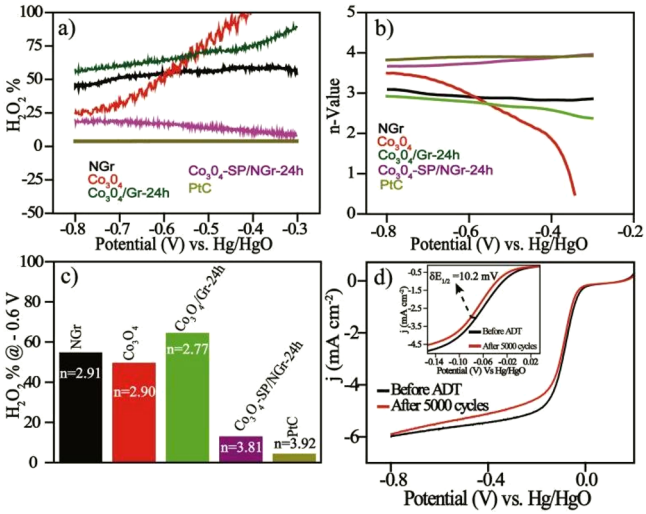

Figure 7. Electrochemical RRDE analysis: (a, b) plots for the percentage of peroxide formation and the electron transfer number of NGr, Co_3O_4, Co_3O_4/Gr-24h, Co_3O_4−SP/NGr-24h, and PtC versus the potential, (c) percentage of hydrogen peroxide and the number of electron transfer calculated at −0.60 V (vs. Hg/HgO), and (d) comparative LSVs of Co_3O_4−SP/NGr-24h catalyst before and after the 5000 potential cycles (inset: enlarged view of the half wave potential region).

facilitates the oxygen reduction reaction through the undesired 2-electron pathway, which leads to hydrogen peroxide (H_2O_2) as the product, the ring electrode in an RRDE can be used to quantify this species. The ring current in Figure S8 corresponds to the formation of H_2O_2, which shows an increase in its yield in the kinetic region and exhibits a steady increase in the diffusion region (<−0.20 V, vs Hg/HgO). Moreover, the ring current starts to decline slightly at higher negative potentials (−0.20 V vs. Hg/HgO) (Figure S9). This could be due to the variation in the number of electrons involved with respect to the potential of the disc electrode during ORR (Figure 7c). Figure 7a depicts how the amount of H_2O_2 (given in %) has been changed with respect to the applied potential. The estimated H_2O_2 yield is found to be significantly high for Co_3O_4 (75%) and Co_3O_4/Gr-24h (nearly 50%), whereas in the case of Co_3O_4−SP/NGr-24h, the amount is found to be in a significantly low level of 16% in the potential region of −0.30 to −0.80 V (vs. Hg/HgO) (Figure 7a). The derived electron transfer numbers from the RRDE estimation are found to be 3.75 and 3.92 for Co_3O_4−SP/NGr-24h and PtC, respectively (Figure 7c), indicating the greater contribution by the direct 4e$^-$ transfer reaction in the reduction of molecular oxygen. Thus, there is a close correlation in the obtained number of electrons as calculated from RRDE and RDE for the ORR process over the system.

To examine the electrochemical stability of the best catalyst, Co_3O_4−SP/NGr-24h and PtC were cycled between the potential range of 0.20 and −0.20 V at 100 mV/s in O_2-saturated 0.1 M KOH. Very less change in the nature of the polarization profile can be seen in the cyclic voltammograms recorded before and after the potential cycling (Figure S10), indicating that the surface properties of the catalysts are retained intact during the cycling. As shown in Figure 7d and Figure S11, the changes in $E_{1/2}$ (∼10.2 mV) after the 5000 continuous potential cycling are found to be 10.2 and 38.2 mV for Co_3O_4−SP/NGr-24h and PtC, respectively (Figure S11), which indicate the better structural integrity of the former under the rigorous electrochemical condition. Nanoparticle migration, coalescence and even detachment from the carbon supports under the exposure of the electrochemical testing environment are known to be the inherent issues associated with the existing PtC catalysts. This stability issue is especially prominent in the case of the alkaline fuel cells and metal−air batteries and this still remains as a major challenge for the widespread implementation of these technologies.[73−75]

Looking at the best performance of Co_3O_4−SP/NGr-24h with better stability during ORR in alkaline condition, we have demonstrated a ZAB by employing this catalyst as the cathode. In this case, a Teflon-coated carbon paper modified with Co_3O_4−SP/NGr-24h was used as the cathode and a Zn foil was employed as the anode. Moreover, the obtained performance with the system derived from Co_3O_4−SP/NGr-24h has been compared with a similar system made from the PtC-derived air electrode. The measured open-circuit voltages for the systems made from Co_3O_4−SP/NGr-24h (1.52 V) and PtC (1.48 V) (Figure 8 and Figure S12) are consistent with the values reported for the batteries in the literatures (Table S2). The comparative steady-state cell polarization (Figure 8b) shows peak power densities of ∼190 and 200 mW/cm^2 for the electrodes derived respectively from Co_3O_4−SP/NGr-24h and

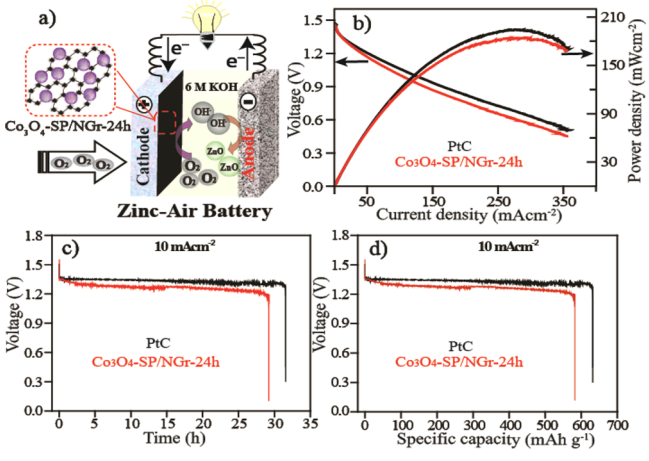

Figure 8. Zn−air battery (ZAB) performance of the catalysts: (a) schematic representation of the fabricated ZAB (catalyst loading: cathode: 1.0 mg/cm^2; anode: zinc foil), (b) polarization plots of the ZABs made with Co_3O_4−SP/NGr-24h and PtC as the air catalysts, (c) long-time galvanostatic discharge curves of the ZABs with Co_3O_4−SP/NGr-24h and PtC as the cathode catalysts until complete consumption of the Zn anode, and (d) specific capacity calculated from the data of c normalized with the mass of the consumed Zn.

DOI: 10.1021/acsami.5b04865
ACS Appl. Mater. Interfaces 2015, 7, 21138−21149

PtC under the identical conditions of the cells. The slight difference in the ORR activity of the cells derived from these two air electrodes could be directly correlated to the previously observed difference in the overall electrochemical performance in the three-electrode system performed in 0.1 M KOH solution. To investigate the robustness of the system made from the Co_3O_4−SP/NGr-24h catalyst, we recorded galvanostatic discharge curves at different discharge current density (10, 20, and 50 mA/cm^2) (Figure S12). Figure 8c, d clearly reveals that the performance of the Co_3O_4−SP/NGr-24h-based ZAB is comparable to the PtC-based system with the same mass loading. The performance of the present system is found to be even higher in comparison to the most of the reported systems based on nonprecious metal electrocatalysts (Table S2). It should be noted that the real cell validation displays a performance characteristics which is consistent with the RDE and RRDE half-cell results of Co_3O_4−SP/NGr-24h.

The primary ZAB performance of the as prepared Co_3O_4−SP/NGr-24h sample is found to be very competitive to the PtC based system even at higher discharge rates (Figure S12). The setup fabricated with Co_3O_4−SP/NGr-24 h as the air electrode has shown ∼30 h of steady flat discharge profile at a discharge current density of 10 mA/cm^2. The performance displayed in this case has very close resemblance with the performance characteristics of the system made from the PtC derived electrode. A similar competitive behavior between the systems has also been observed at the higher discharge rates of 20 and 50 mA/cm^2. It is also worth noting that the potential drop from the system is found to be very small during the long-term galvanostatic discharge profile measurements (Figure 8c). The calculated specific capacity (Figure 8d) of the primary ZAB is found to be ∼590 mAh/g_{-Zn}, whereas the PtC derived setup shows a specific capacity of ∼620 mAh/g_{-Zn}. The obtained values thus indicate the close activity of Co_3O_4−SP/NGr-24h with PtC. Moreover, both the systems show lowering of cell potential with increasing the discharge current rate because of the formation of the insulating Zn-oxide on the pristine Zn anode (Figure 8c, d and Figure S12), an adverse effect which is already reported in the literatures.[8,14,76,77] Furthermore, we have carried out a real time demonstration of the fabricated ZAB by lighting up 20 LEDs. For lighting the LEDs, we have connected two ZABs in series which show an OCP of ∼3.14 V. We found that the LEDs (20 numbers) are lighting up to 8 h without much loss of intensity (shown in Figure 9 and Video S1, showing the continuous luminous recorded for 10 min).

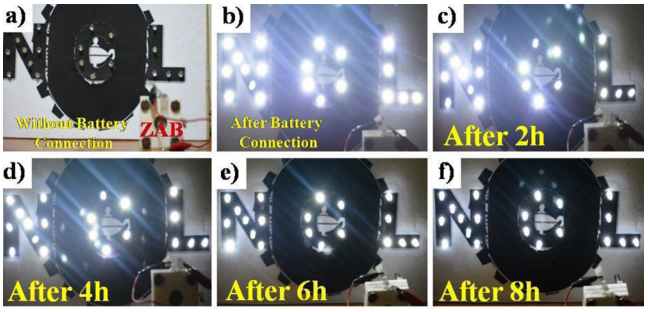

Figure 9. Demonstration of the assembled ZAB: (a) digital photograph of 20 LEDs without connection to the assembled ZAB, (b–f) digital photograph of the lighting LEDs connected with ZAB recorded at different time intervals.

Interestingly, after the complete discharge of the battery, it could be again recharged by refueling the anode (i.e., Zn) and the electrolyte periodically. In this way, the cathode electrode made with Co_3O_4−SP/NGr-24h could work robustly for more than 20 h at a higher discharge current density (50 mA/cm^2) with minimal voltage loss (Figure 10), highlighting the high

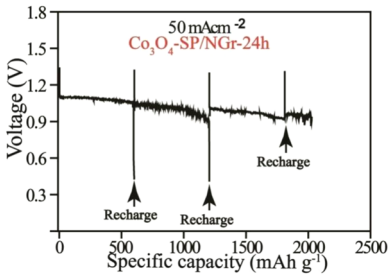

Figure 10. Recharging of the ZAB, using Co_3O_4−SP/NGr-24h catalyst as the cathode material and by reloading the Zn anode and electrolyte regularly. The recharging process is indicated by the arrows. Conditions: electrolyte: 6 M KOH, discharge rate: 50 mA/cm^2, anode: Zn-foil, cathode: Co_3O_4−SP/NGr-24 h derived catalyst.

stability of the Co_3O_4−SP/NGr-24h-based ZAB setup. Thus, the robustness of Co_3O_4−SP/NGr-24h as the air electrode in terms of activity and stability stands out as a strong aspect of the system to find a special place in future metal−air battery applications.

4. CONCLUSION

In conclusion, the manuscript deals with the synthesis of a prospective non-noble metal based ORR electrocatalyst derived by the dispersion of surface tuned Co_3O_4 nanoparticles on NGr by employing a simple hydrothermal method. The reaction condition of the hydrothermal method is found to be playing a vital role in tuning the structural and morphological features of the Co_3O_4 nanoparticles. The doped nitrogen also plays a critical role as a supporting material to ensure good dispersion of the oxide nanoparticles and in bringing in favorable activity modulation in the system. We found that the spherical Co_3O_4 nanoparticle-supported NGr catalyst (Co_3O_4−SP/NGr-24h) has acquired a significant activity makeover to display an ORR activity that is closely matched with the state-of-the-art Pt-supported carbon (PtC) catalyst in alkaline medium. This activity enhancement has been originated by the controlled interplay of multiple favoring factors in the system, which includes the high roughness factor of Co_3O_4, increased surface area of the catalyst, homogeneous dispersion of the oxide nanoparticles and synergetic interaction between the doped nitrogen and the Co_3O_4 nanoparticles. Co_3O_4−SP/NGr-24h has shown ∼5.4 and ∼6.0 times improved mass activity for ORR in comparison to Co_3O_4 and Gr/NGr, respectively. Moreover, the performance of the ZAB fabricated by using Co_3O_4−SP/NGr-24h-coated carbon paper as the cathode is found to be closely matching with the performance of the system derived from the state-of-the-art PtC as the cathode. The Co_3O_4−SP/NGr-24h based system has shown comparable specific capacity and power density to its PtC counterpart. The robustness of the Co_3O_4−SP/NGr-24h-based system could be tested with mechanically rechargeable ZAB, which displayed good stability characteristics throughout the testing.

DOI: 10.1021/acsami.5b04865
ACS Appl. Mater. Interfaces 2015, 7, 21138−21149

■ ASSOCIATED CONTENT

Supporting Information

[The Supporting Information is available free of charge on the ACS Publications website at DOI: 10.1021/acsami.5b04865.

Details of experimental of RRDE, TGA, CV of Co_3O_4-/NGr-xh catalysts, C 1s, XPS of NGr, particle size histogram of Co_3O_4/Gr-24h, Co_3O_4/NGr-*x*h (x = 9, 12, 24 and 48) (PDF)

Video S1 (AVI)

■ AUTHOR INFORMATION

Corresponding Author

*E-mail: k.sreekumar@ncl.res.in.

Author Contributions

The manuscript was written through contributions of all the authors. All the authors have given approval to the final version of the manuscript.

Funding

This study was financially supported by Council of Scientific and Industrial Research (CSIR), New Delhi, India, by project funding (CSC 0122) to S.K. and research fellowship to S.K.S.

Notes

The authors declare no competing financial interest.

■ ACKNOWLEDGMENTS

S.K.S. and K.S. acknowledge CSIR for the research fellowship to S.K.S. and project funding (CSC 0122) to K.S..

■ REFERENCES

(1) Shukla, A. K.; Kumar, T. P. Lithium Economy: Will It Get the Electric Traction? *J. Phys. Chem. Lett.* **2013**, *4*, 551−555.

(2) Kendall, A.; Price, L. Incorporating Time-Corrected Life Cycle Greenhouse Gas Emissions in Vehicle Regulations. *Environ. Sci. Technol.* **2012**, *46*, 2557−2563.

(3) Wagner, F. T.; Lakshmanan, B.; Mathias, M. F. Electrochemistry and the Future of the Automobile. *J. Phys. Chem. Lett.* **2010**, *1*, 2204−2219.

(4) Kim, H.; Boysen, D. A.; Newhouse, J. M.; Spatocco, B. L.; Chung, B.; Burke, P. J.; Bradwell, D. J.; Jiang, K.; Tomaszowska, A. A.; Wang, K.; Wei, W.; Ortiz, L. A.; Barriga, S. A.; Poizeau, S. M.; Sadoway, D. R. Liquid Metal Batteries: Past, Present, and Future. *Chem. Rev.* **2013**, *113*, 2075−2099.

(5) McCloskey, B. D.; Bethune, D. S.; Shelby, R. M.; Mori, T.; Scheffler, R.; Speidel, A.; Sherwood, M.; Luntz, A. C. Limitations in Rechargeability of Li-O_2 Batteries and Possible Origins. *J. Phys. Chem. Lett.* **2012**, *3*, 3043−3047.

(6) Abraham, K. M. Prospects and Limits of Energy Storage in Batteries. *J. Phys. Chem. Lett.* **2015**, *6*, 830−844.

(7) Whittingham, M. S. Ultimate Limits to Intercalation Reactions for Lithium Batteries. *Chem. Rev.* **2014**, *114*, 11414−11443.

(8) Neburchilov, V.; Wang, H.; Martin, J. J.; Qu, W. A Review on Air Cathodes for Zinc−Air Fuel Cells. *J. Power Sources* **2010**, *195*, 1271−1291.

(9) Cheng, F.; Shen, J.; Peng, B.; Pan, Y.; Tao, Z.; Chen, J. Rapid Room-Temperature Synthesis of Nanocrystalline Spinels as Oxygen Reduction and Evolution Electrocatalysts. *Nat. Chem.* **2011**, *3*, 79−84.

(10) Rahman, M. A.; Wang, X.; Wen, C. High Energy Density Metal-Air Batteries: A Review. *J. Electrochem. Soc.* **2013**, *160*, A1759−A1771.

(11) Cao, R.; Lee, J.-S.; Liu, M.; Cho, J. Recent Progress in Non-Precious Catalysts for Metal-Air Batteries. *Adv. Energy Mater.* **2012**, *2*, 816−829.

(12) Prabu, M.; Ramakrishnan, P.; Nara, H.; Momma, T.; Osaka, T.; Shanmugam, S. Zinc−Air Battery: Understanding the Structure and Morphology Changes of Graphene-Supported $CoMn_2O_4$ Bifunctional Catalysts Under Practical Rechargeable Conditions. *ACS Appl. Mater. Interfaces* **2014**, *6*, 16545−16555.

(13) Cao, R.; Thapa, R.; Kim, H.; Xu, X.; Gyu Kim, M.; Li, Q.; Park, N.; Liu, M.; Cho, J. Promotion of Oxygen Reduction by a Bio-inspired Tethered Iron Phthalocyanine Carbon Nanotube-Based Catalyst. *Nat. Commun.* **2013**, *4*, 1−7.

(14) Lee, J.-S.; Tai Kim, S.; Cao, R.; Choi, N.-S.; Liu, M.; Lee, K. T.; Cho, J. Metal−Air Batteries with High Energy Density: Li−Air Versus Zn−Air. *Adv. Energy Mater.* **2011**, *1*, 34−50.

(15) Lee, D. U.; Choi, J.-Y.; Feng, K.; Park, H. W.; Chen, Z. Advanced Extremely Durable 3D Bifunctional Air Electrodes for Rechargeable Zinc-Air Batteries. *Adv. Energy Mater.* **2014**, *4*, DOI: 10.1002/aenm.201301389.

(16) Pei, P.; Wang, K.; Ma, Z. Technologies for Extending Zinc−Air Battery's Cyclelife: A Review. *Appl. Energy* **2014**, *128*, 315−324.

(17) Parker, J. F.; Chervin, C. N.; Nelson, E. S.; Rolison, D. R.; Long, J. W. Wiring Zinc in Three Dimensions Re-Writes Battery Performance-Dendrite-Free Cycling. *Energy Environ. Sci.* **2014**, *7*, 1117−1124.

(18) Pei, P.; Ma, Z.; Wang, K.; Wang, X.; Song, M.; Xu, H. High Performance Zinc Air Fuel Cell Stack. *J. Power Sources* **2014**, *249*, 13−20.

(19) McLarnon, F. R.; Cairns, E. J. The Secondary Alkaline Zinc Electrode. *J. Electrochem. Soc.* **1991**, *138*, 645−656.

(20) Du, G.; Liu, X.; Zong, Y.; Hor, T. S. A.; Yu, A.; Liu, Z. Co_3O_4 Nanoparticle-Modified MnO_2 Nanotube Bifunctional Oxygen Cathode Catalysts for Rechargeable Zinc-Air Batteries. *Nanoscale* **2013**, *5*, 4657−4661.

(21) Chen, Z.; Yu, A.; Higgins, D.; Li, H.; Wang, H.; Chen, Z. Highly Active and Durable Core−Corona Structured Bifunctional Catalyst for Rechargeable Metal−Air Battery Application. *Nano Lett.* **2012**, *12*, 1946−1952.

(22) Lee, J.-S.; Park, G. S.; Lee, H. I.; Kim, S. T.; Cao, R.; Liu, M.; Cho, J. Ketjenblack Carbon Supported Amorphous Manganese Oxides Nanowires as Highly Efficient Electrocatalyst for Oxygen Reduction Reaction in Alkaline Solutions. *Nano Lett.* **2011**, *11*, 5362−5366.

(23) Nam, G.; Park, J.; Kim, S. T.; Shin, D.-b.; Park, N.; Kim, Y.; Lee, J.-S.; Cho, J. Metal-Free Ketjenblack Incorporated Nitrogen-Doped Carbon Sheets Derived from Gelatin as Oxygen Reduction Catalysts. *Nano Lett.* **2014**, *14*, 1870−1876.

(24) Liang, H.-W.; Zhuang, X.; Brüller, S.; Feng, X.; Müllen, K. Hierarchically Porous Carbons with Optimized Nitrogen Doping as Highly Active Electrocatalysts for Oxygen Reduction. *Nat. Commun.* **2014**, *5*, 4973.

(25) Lee, D. U.; Scott, J.; Park, H. W.; Abureden, S.; Choi, J.-Y.; Chen, Z. Morphologically Controlled Co_3O_4 Nanodisks as Practical Bi-functional Catalyst for Rechargeable Zinc−Air Battery Applications. *Electrochem. Commun.* **2014**, *43*, 109−112.

(26) Li, Y.; Gong, M.; Liang, Y.; Feng, J.; Kim, J.-E.; Wang, H.; Hong, G.; Zhang, B.; Dai, H. Advanced Zinc-Air Batteries Based on High-Performance Hybrid Electrocatalysts. *Nat. Commun.* **2013**, *4*, 1805.

(27) Ge, X.; Liu, Y.; Goh, F. W. T.; Hor, T. S. A.; Zong, Y.; Xiao, P.; Zhang, Z.; Lim, S. H.; Li, B.; Wang, X.; Liu, Z. Dual-Phase Spinel $MnCo_2O_4$ and Spinel $MnCo_2O_4$/Nanocarbon Hybrids for Electrocatalytic Oxygen Reduction and Evolution. *ACS Appl. Mater. Interfaces* **2014**, *6*, 12684−12691.

(28) Dhavale, V. M.; Kurungot, S. Cu−Pt Nanocage with 3-D Electrocatalytic Surface as an Efficient Oxygen Reduction Electrocatalyst for a Primary Zn−Air Battery. *ACS Catal.* **2015**, *5*, 1445−1452.

(29) Fei, H.; Ye, R.; Ye, G.; Gong, Y.; Peng, Z.; Fan, X.; Samuel, E. L. G.; Ajayan, P. M.; Tour, J. M. Boron- and Nitrogen-Doped Graphene Quantum Dots/Graphene Hybrid Nanoplatelets as Efficient Electrocatalysts for Oxygen Reduction. *ACS Nano* **2014**, *8*, 10837−10843.

(30) Kong, X.-K.; Chen, C.-L.; Chen, Q.-W. Doped Graphene for Metal-Free Catalysis. *Chem. Soc. Rev.* **2014**, *43*, 2841−2857.

(31) Guo, Z.; Jiang, C.; Teng, C.; Ren, G.; Zhu, Y.; Jiang, L. Sulfur, Trace Nitrogen and Iron Codoped Hierarchically Porous Carbon Foams as Synergistic Catalysts for Oxygen Reduction Reaction. *ACS Appl. Mater. Interfaces* **2014**, *6*, 21454−21460.

(32) Paraknowitsch, J. P.; Zhang, Y.; Wienert, B.; Thomas, A. Nitrogen and Phosphorus-co-Doped Carbons with Tunable Enhanced Surface Areas Promoted by the Doping Additives. *Chem. Commun.* **2013**, *49*, 1208−1210.
(33) Qu, L.; Liu, Y.; Baek, J.-B.; Dai, L. Nitrogen-Doped Graphene as Efficient Metal-Free Electrocatalyst for Oxygen Reduction in Fuel Cells. *ACS Nano* **2010**, *4*, 1321−1326.
(34) Usachov, D.; Fedorov, A.; Vilkov, O.; Senkovskiy, B.; Adamchuk, V. K.; Yashina, L. V.; Volykhov, A. A.; Farjam, M.; Verbitskiy, N. I.; Grüneis, A.; Laubschat, C.; Vyalikh, D. V. The Chemistry of Imperfections in N-Graphene. *Nano Lett.* **2014**, *14*, 4982−4988.
(35) Pham, V. D.; Lagoute, J.; Mouhoub, O.; Joucken, F.; Repain, V.; Chacon, C.; Bellec, A.; Girard, Y.; Rousset, S. Electronic Interaction Between Nitrogen-Doped Graphene and Porphyrin Molecules. *ACS Nano* **2014**, *8*, 9403−9409.
(36) Ge, X.; Sumboja, A.; Wuu, D.; An, T.; Li, B.; Goh, F. W. T.; Hor, T. S. A.; Zong, Y.; Liu, Z. Oxygen Reduction in Alkaline Media: From Mechanisms to Recent Advances of Catalysts. *ACS Catal.* **2015**, *5*, 4643−4667.
(37) Lv, L.-B.; Ye, T.-N.; Gong, L.-H.; Wang, K.-X.; Su, J.; Li, X.-H.; Chen, J.-S. Anchoring Cobalt Nanocrystals Through the Plane of Graphene: Highly Integrated Electrocatalyst for Oxygen Reduction Reaction. *Chem. Mater.* **2015**, *27*, 544−549.
(38) He, Q.; Li, Q.; Khene, S.; Ren, X.; Lopez-Suarez, F. E.; Lozano-Castello, D.; Bueno-Lopez, A.; Wu, G. High-Loading Cobalt Oxide Coupled with Nitrogen-Doped Graphene for Oxygen Reduction in Anion-Exchange-Membrane Alkaline Fuel Cells. *J. Phys. Chem. C* **2013**, *117*, 8697−8707.
(39) Ge, X.; Goh, F. W. T.; Li, B.; Hor, T. S. A.; Zhang, J.; Xiao, P.; Wang, X.; Zong, Y.; Liu, Z. Efficient and Durable Oxygen Reduction and Evolution of a Hydrothermally Synthesized La-$(Co_{0.55}Mn_{0.45})_{0.99}O_{3-\delta}$ Nanorod/Graphene Hybrid in Alkaline Media. *Nanoscale* **2015**, *7*, 9046−9054.
(40) Wu, J.; Xue, Y.; Yan, X.; Yan, W.; Cheng, Q.; Xie, Y. Co_3O_4 Nanocrystals on Single-Walled Carbon Nanotubes as a Highly Efficient Oxygen-Evolving Catalyst. *Nano Res.* **2012**, *5*, 521−530.
(41) Liang, Y.; Wang, H.; Zhou, J.; Li, Y.; Wang, J.; Regier, T.; Dai, H. Covalent Hybrid of Spinel Manganese−Cobalt Oxide and Graphene as Advanced Oxygen Reduction Electrocatalysts. *J. Am. Chem. Soc.* **2012**, *134*, 3517−3523.
(42) Bahlawane, N.; Ngamou, P. H. T.; Vannier, V.; Kottke, T.; Heberle, J.; Kohse-Hoinghaus, K. Tailoring the Properties and the Reactivity of the Spinel Cobalt Oxide. *Phys. Chem. Chem. Phys.* **2009**, *11*, 9224−9232.
(43) Li, B.; Ge, X.; Goh, F. W. T.; Hor, T. S. A.; Geng, D.; Du, G.; Liu, Z.; Zhang, J.; Liu, X.; Zong, Y. Co_3O_4 Nanoparticles Decorated Carbon Nanofiber Mat as Binder-Free Air-Cathode for High Performance Rechargeable Ainc-Air Batteries. *Nanoscale* **2015**, *7*, 1830−1838.
(44) Singh, S. K.; Dhavale, V. M.; Kurungot, S. Low Surface Energy Plane Exposed Co_3O_4 Nanocubes Supported on Nitrogen-Doped Graphene as an Electrocatalyst for Efficient Water Oxidation. *ACS Appl. Mater. Interfaces* **2015**, *7*, 442−451.
(45) Xiao, J.; Kuang, Q.; Yang, S.; Xiao, F.; Wang, S.; Guo, L. Surface Structure Dependent Electrocatalytic Activity of Co_3O_4 Anchored on Graphene Sheets toward Oxygen Reduction Reaction. *Sci. Rep.* **2013**, *3*, 1−8.
(46) Yang, G.; Li, L.; Rana, R. K.; Zhu, J.-J. Assembled Gold Nanoparticles on Nitrogen-Doped Graphene for Ultrasensitive Electrochemical Detection of Matrix Metalloproteinase-2. *Carbon* **2013**, *61*, 357−366.
(47) Wu, P.; Huang, Y.; Zhou, L.; Wang, Y.; Bu, Y.; Yao, J. Nitrogen-Doped Graphene Supported Highly Dispersed Palladium-lead Nanoparticles for Synergetic Enhancement of Ethanol Electrooxidation in Alkaline Medium. *Electrochim. Acta* **2015**, *152*, 68−74.
(48) Liang, Y.; Li, Y.; Wang, H.; Zhou, J.; Wang, J.; Regier, T.; Dai, H. Co_3O_4 Nanocrystals on Graphene as a Synergistic Catalyst for Oxygen Reduction Reaction. *Nat. Mater.* **2011**, *10*, 780−786.
(49) Dhavale, V. M.; Gaikwad, S. S.; George, L.; Devi, R. N.; Kurungot, S. Nitrogen-Doped Graphene Interpenetrated 3D Ni-nanocages: Efficient and Stable Water-to-Dioxygen Electrocatalysts. *Nanoscale* **2014**, *6*, 13179−13187.
(50) Wang, Y.; Lei, Y.; Li, J.; Gu, L.; Yuan, H.; Xiao, D. Synthesis of 3D-Nanonet Hollow Structured Co_3O_4 for High Capacity Supercapacitor. *ACS Appl. Mater. Interfaces* **2014**, *6*, 6739−6747.
(51) Huang, H.; Zhu, W.; Tao, X.; Xia, Y.; Yu, Z.; Fang, J.; Gan, Y.; Zhang, W. Nanocrystal-Constructed Mesoporous Single-Crystalline Co_3O_4 Nanobelts with Superior Rate Capability for Advanced Lithium-Ion Batteries. *ACS Appl. Mater. Interfaces* **2012**, *4*, 5974−5980.
(52) Liu, D.; Wang, X.; Wang, X.; Tian, W.; Bando, Y.; Golberg, D. Co_3O_4 Nanocages with Highly Exposed {110} Facets for High-Performance Lithium Storage. *Sci. Rep.* **2013**, *3*, 1−6.
(53) Sa, Y. J.; Kwon, K.; Cheon, J. Y.; Kleitz, F.; Joo, S. H. Ordered Mesoporous Co_3O_4 Spinels as Stable, Bifunctional, Noble Metal-Free Oxygen Electrocatalysts. *J. Mater. Chem. A* **2013**, *1*, 9992−10001.
(54) Unni, S. M.; Devulapally, S.; Karjule, N.; Kurungot, S. Graphene Enriched with Pyrrolic Coordination of the Doped Nitrogen as an Efficient Metal-Free Electrocatalyst for Oxygen Reduction. *J. Mater. Chem.* **2012**, *22*, 23506−23513.
(55) Palaniselvam, T.; Valappil, M. O.; Illathvalappil, R.; Kurungot, S. Nanoporous Graphene by Quantum Dots Rremoval from Graphene and its Conversion to a Potential Oxygen Reduction Electrocatalyst via Nitrogen Doping. *Energy Environ. Sci.* **2014**, *7*, 1059−1067.
(56) Xie, X.; Li, Y.; Liu, Z.-Q.; Haruta, M.; Shen, W. Low-Temperature Oxidation of CO catalysed by Co_3O_4 Nanorods. *Nature* **2009**, *458*, 746−749.
(57) Dubau, L.; Asset, T.; Chattot, R.; Bonnaud, C.; Vanpeene, V.; Nelayah, J.; Maillard, F. Tuning the Performance and the Stability of Porous Hollow PtNi/C Nanostructures for the Oxygen Reduction Reaction. *ACS Catal.* **2015**, *5*, 5333−5341.
(58) Ziegelbauer, J. M.; Olson, T. S.; Pylypenko, S.; Alamgir, F.; Jaye, C.; Atanassov, P.; Mukerjee, S. Direct Spectroscopic Observation of the Structural Origin of Peroxide Generation from Co-Based Pyrolyzed Porphyrins for ORR Applications. *J. Phys. Chem. C* **2008**, *112*, 8839−8849.
(59) Artyushkova, K.; Pylypenko, S.; Olson, T. S.; Fulghum, J. E.; Atanassov, P. Predictive Modeling of Electrocatalyst Structure Based on Structure-to-Property Correlations of X-ray Photoelectron Spectroscopic and Electrochemical Measurements. *Langmuir* **2008**, *24*, 9082−9088.
(60) Yang, J.; Liu, H.; Martens, W. N.; Frost, R. L. Synthesis and Characterization of Cobalt Hydroxide, Cobalt Oxyhydroxide, and Cobalt Oxide Nanodiscs. *J. Phys. Chem. C* **2010**, *114*, 111−119.
(61) Ganguly, A.; Sharma, S.; Papakonstantinou, P.; Hamilton, J. Probing the Thermal Deoxygenation of Graphene Oxide Using High-Resolution In Situ X-ray-Based Spectroscopies. *J. Phys. Chem. C* **2011**, *115*, 17009−17019.
(62) Wang, W. X.; Liang, S. H.; Yu, T.; Li, D. H.; Li, Y. B.; Han, X. F. The Study of Interaction Between Graphene and Metals by Raman Spectroscopy. *J. Appl. Phys.* **2011**, *109*, 07C501.
(63) Ferrari, A. C.; Meyer, J. C.; Scardaci, V.; Casiraghi, C.; Lazzeri, M.; Mauri, F.; Piscanec, S.; Jiang, D.; Novoselov, K. S.; Roth, S.; Geim, A. K. Raman Spectrum of Graphene and Graphene Layers. *Phys. Rev. Lett.* **2006**, *97*, 187401.
(64) Yan, J.; Zhang, Y.; Kim, P.; Pinczuk, A. Electric Field Effect Tuning of Electron-Phonon Coupling in Graphene. *Phys. Rev. Lett.* **2007**, *98*, 166802.
(65) Das, A.; Pisana, S.; Chakraborty, B.; Piscanec, S.; Saha, S. K.; Waghmare, U. V.; Novoselov, K. S.; Krishnamurthy, H. R.; Geim, A. K.; Ferrari, A. C.; Sood, A. K. Monitoring Dopants by Raman Scattering in an Electrochemically Top-gated Graphene Transistor. *Nat. Nanotechnol.* **2008**, *3*, 210−215.
(66) Hulman, M.; Haluška, M.; Scalia, G.; Obergfell, D.; Roth, S. Effects of Charge Impurities and Laser Energy on Raman Spectra of Graphene. *Nano Lett.* **2008**, *8*, 3594−3597.

DOI: 10.1021/acsami.5b04865
ACS Appl. Mater. Interfaces 2015, 7, 21138−21149

(67) Mohiuddin, T. M. G.; Lombardo, A.; Nair, R. R.; Bonetti, A.; Savini, G.; Jalil, R.; Bonini, N.; Basko, D. M.; Galiotis, C.; Marzari, N.; Novoselov, K. S.; Geim, A. K.; Ferrari, A. C. Uniaxial Strain in Graphene by Raman Spectroscopy: "G" Peak Splitting, Gruneisen Parameters, and Sample Orientation. *Phys. Rev. B: Condens. Matter Mater. Phys.* **2009**, *79*, 205433.
(68) Zhao, Y.; Chen, S.; Sun, B.; Su, D.; Huang, X.; Liu, H.; Yan, Y.; Sun, K.; Wang, G. Graphene-Co_3O_4 Nanocomposite as Electrocatalyst with High Performance for Oxygen Evolution Reaction. *Sci. Rep.* **2015**, *5*, 76269.
(69) Qiu, Y.; Xin, L.; Li, W. Electrocatalytic Oxygen Evolution over Supported Small Amorphous Ni−Fe Nanoparticles in Alkaline Electrolyte. *Langmuir* **2014**, *30*, 7893−7901.
(70) McCrory, C. C. L.; Jung, S.; Peters, J. C.; Jaramillo, T. F. Benchmarking Heterogeneous Electrocatalysts for the Oxygen Evolution Reaction. *J. Am. Chem. Soc.* **2013**, *135*, 16977−16987.
(71) Wei, G.-F.; Fang, Y.-H.; Liu, Z.-P. First Principles Tafel Kinetics for Resolving Key Parameters in Optimizing Oxygen Electrocatalytic Reduction Catalyst. *J. Phys. Chem. C* **2012**, *116*, 12696−12705.
(72) Fang, Y.-H.; Liu, Z.-P. Tafel Kinetics of Electrocatalytic Reactions: From Experiment to First-Principles. *ACS Catal.* **2014**, *4*, 4364−4376.
(73) Gewirth, A. A.; Thorum, M. S. Electroreduction of Dioxygen for Fuel-Cell Applications: Materials and Challenges. *Inorg. Chem.* **2010**, *49*, 3557−3566.
(74) Li, Y.; Zhou, W.; Wang, H.; Xie, L.; Liang, Y.; Wei, F.; Idrobo, J.-C.; Pennycook, S. J.; Dai, H. An Oxygen Reduction Electrocatalyst Based on Carbon Nanotube-Graphene Complexes. *Nat. Nanotechnol.* **2012**, *7*, 394−400.
(75) Guo, J.; Hsu, A.; Chu, D.; Chen, R. Improving Oxygen Reduction Reaction Activities on Carbon-Supported Ag Nanoparticles in Alkaline Solutions. *J. Phys. Chem. C* **2010**, *114*, 4324−4330.
(76) Zhu, A. L.; Duch, D.; Roberts, G. A.; Li, S. X. X.; Wang, H.; Duch, K.; Bae, E.; Jung, K. S.; Wilkinson, D.; Kulinich, S. A. Increasing the Electrolyte Capacity of Alkaline Zn−Air Fuel Cells by Scavenging Zincate with $Ca(OH)_2$. *ChemElectroChem* **2015**, *2*, 134−142.
(77) Siahrostami, S.; Tripkovic, V.; Lundgaard, K. T.; Jensen, K. E.; Hansen, H. A.; Hummelshoj, J. S.; Myrdal, J. S. G.; Vegge, T.; Norskov, J. K.; Rossmeisl, J. First Principles Investigation of Zinc-Anode Dissolution in Zinc-Air Batteries. *Phys. Chem. Chem. Phys.* **2013**, *15*, 6416−6421.

DOI: 10.1021/acsami.5b04865
ACS Appl. Mater. Interfaces 2015, 7, 21138−21149